

The degeneracy between microlensing and spin precession in strongly-lensed binary black hole events

3 XIKAI SHAN ,¹ HUAN YANG ,¹ SHUDE MAO ,² AND OTTO HANNUKSELA ,³

4 ¹*Department of Astronomy, Tsinghua University, Beijing 100084, China*

5 ²*Department of Astronomy, Westlake University, Hangzhou 310030, Zhejiang Province, China*

6 ³*Department of Physics, The Chinese University of Hong Kong, Shatin, NT, Hong Kong*

ABSTRACT

Microlensing induced by the stellar field within a strong lensing galaxy can introduce fluctuations in the waveforms of strongly-lensed gravitational waves (SLGWs), e.g. binary black holes. When fitting these signals with templates that do not account for microlensing, possible degeneracies can lead to false evidence of certain intrinsic parameters, resulting in a misinterpretation of the properties of the underlying system. For example, the wave effect of microlensing may mimic spin precessions, as both effects generically induce periodic waveform modulations. Although previous studies suggest that lensing-induced modulations can be distinguished from precession using parameter estimation under a geometric-optic approximation, it does not directly apply for lensed image through stellar fields due to large number of stars involved an wave-optic effects. This study aims to evaluate the degree of degeneracy between the stellar-field microlensing and spin precession, investigating whether microlensing leads false evidence of precession. In other words, to what extent observed SLGWs are identified with false evidence of precession. The main findings are as follows. First, assuming O5 sensitivity and parallel spins for the underlying binary black holes, microlensing-induced false evidence of precession is generally weak (15% of the events show significant evidence, 30% if the signal-to-noise ratio doubles). Second, for highly magnified events (magnification $\mu \simeq 100$), about 72% of the population show significant evidence of precession, which could serve as an identification criterion for microlensing. Finally, a moderate to strong positive correlation exists between microlensing strength and precession evidence, more pronounced in Type II (saddle images) SLGWs. This suggests that stronger precession evidence may imply a stronger microlensing effect.

27 *Keywords:* Gravitational wave — Gravitational lensing — Microlensing — Strong lensing

1. INTRODUCTION

29 Strongly-lensed gravitational waves (SLGWs) offer a new method for probing the Universe (Li et al. 2018; Oguri
30 2019; Hannuksela et al. 2020; Liao et al. 2022). Unlike strongly lensed quasars or supernovae, the characteristic
31 GW wavelength of these transient events, i.e. binary black hole coalescence, may be comparable to the lens mass as
32 the images pass through a stellar field within the lensing galaxy, introducing additional interference and diffraction
33 effects (Nakamura & Deguchi 1999; Nakamura 1998; Takahashi & Nakamura 2003; Diego et al. 2019; Mishra et al.
34 2021; Meena et al. 2022; Seo et al. 2025). By extracting the interference imprints within gravitational waves, it may be
35 possible to reconstruct substructure information of the lens galaxy, such as the properties of intermediate-mass black
36 holes (Lai et al. 2018) and dark matter substructures (Liu et al. 2023).

37 The foundation of the application of strongly lensed gravitational waves relies on the accurate and efficient identifi-
38 cation of such events. However, the two main methods currently available—the overlap method (Haris et al. 2018)
39 and the joint Parameter Estimation (PE) method (Lo & Magaña Hernandez 2021; Liu et al. 2021; Janquart et al.

40—[2021](#))—are susceptible to varying degrees by issues related to false positive rates. Although using population models
 41 to provide priors, such as time delay information, can somewhat alleviate this issue, introducing a novel third-party
 42 criterion would be a valuable contribution to this task.

43 In fact, as a strongly-lensed image passes through the lensing galaxy, it may be further (micro)-lensed by stars or
 44 milli-lensed by more massive intermediate mass black holes and/or Dark Matter sub-halos. It has been observed that
 45 the effects of microlensing on gravitational wave waveforms bear similarities to intrinsic precession effects, with both
 46 producing a beat-pattern-like modulation on the waveform ([Liu & Kim 2024](#)). Although their study demonstrates
 47 that these two effects can be disentangled using template matching, their conclusion is primarily applicable to cases
 48 where template construction is relatively straightforward, such as in the millilensing scenario. For a microlensing field
 49 composed of stars, constructing such templates becomes extremely challenging, due to the large number of microlenses
 50 that need to be considered ([Katz et al. 1986; Shan et al. 2023b](#)). As a result, no waveform templates for stellar-field
 51 microlensing are available. Such templates would offer the most straightforward way to distinguish this effect from
 52 others, such as spin precession. Such microlensing effects may also be mistakenly interpreted as precession effects, if
 53 their waveforms bear certain level of similarities.

54 In this work, we systematically investigate the degeneracies between microlensing wave-optics effects and precession
 55 effects in strongly lensed gravitational waves. Specifically, we quantify the percentage of strongly-lensed events that
 56 would show significant evidence of precession assuming the presence of microlensing and non-precessing underlying
 57 binary systems. We find that microlensing can indeed lead to evidence of precession, depending on the strength of the
 58 microlensing effect and the detector’s sensitivity level. In fact, if a future lower-noise detector detects a high mismatch
 59 microlensing event, e.g., a highly magnified event, there is a high probability that such an event will also be identified
 60 as a precessional binary. Thus, precession may be treated as a third-party criterion for SLGWs.

61 In population studies of binary black holes, mis-identification of precessional systems could lead to incorrect con-
 62 clusions about the formation mechanisms of binary black hole systems, potentially favouring dynamical interaction in
 63 dense clusters (the dynamical channel) ([Sigurdsson & Hernquist 1993; Portegies Zwart & McMillan 2000; Rodriguez](#)
 64 [et al. 2016; Mapelli et al. 2022](#)), as compared to through the evolution of isolated binary stars (the EMBS channel)
 65 ([Abbott et al. 2016; Belczynski et al. 2016; Giacobbo & Mapelli 2018](#)). On the other hand, in the context of
 66 lensing identification, these degeneracies could serve as new evidence for strongly lensed events, as every strongly-lensed
 67 image must be microlensed and more than 10% of events will have microlensing-induced mismatches > 0.03 in the
 68 waveform ([Shan et al. 2025](#)). In other words, if a candidate list of strong-lensing events also show a strong correlation
 69 with spin precession, as compared to average events, the false alarm rate may be further reduced.

70 The structure of the paper is as follows: in Section 2, we introduce the fundamental theories of strong lensing and
 71 microlensing, along with the simulation processes used for the data. Section 3 presents our results, and finally, we
 72 provide a summary and discussion in Section 4.

73 2. BASIC THEORY AND MOCK DATA SIMULATION

74 The gravitational wave (GW) lensing effect induced by a microlensing field embedded within a strong lensing galaxy
 75 can be described through the diffraction integral ([Schneider et al. 1992; Nakamura & Deguchi 1999; Takahashi &](#)
 76 [Nakamura 2003](#)), as described in the following equation:

$$77 F(\omega, \mathbf{y}) = \frac{2G\langle M_L \rangle(1+z_L)\omega}{\pi c^3 i} \int_{-\infty}^{\infty} d^2x \exp[i\omega t(\mathbf{x}, \mathbf{y})]. \quad (1)$$

78 Here, $F(\omega, \mathbf{y})$ represents the amplification factor, while ω and \mathbf{y} denote the GW angular frequency and its position
 79 in the source plane (normalized by the Einstein radius), respectively. $\langle M_L \rangle$ represents the average microlens mass, z_L
 80 refers to the lens redshift, and \mathbf{x} corresponds to the coordinates in the lens plane (normalized by the Einstein radius).

81 In Eq. (1), the term $t(\mathbf{x}, \mathbf{y})$ represents the time delay function for the microlensing field embedded in the lens galaxy
 82 or galaxy cluster, which can be expressed as ([Wambsganss 1990; Schneider et al. 1992; Chen et al. 2021](#)):

$$83 t(\mathbf{x}, \mathbf{x}^i, \mathbf{y} = 0) = \underbrace{\frac{k}{2} ((1 - \kappa + \gamma)x_1^2 + (1 - \kappa - \gamma)x_2^2)}_{t_{\text{smooth}}(\kappa, \gamma, \mathbf{x})} - \underbrace{\left[\frac{k}{2} \sum_i^{N_*} \frac{M_{L,i}}{\langle M_L \rangle} \ln (\mathbf{x}^i - \mathbf{x})^2 + k\phi_-(\mathbf{x}) \right]}_{t_{\text{micro}}(\mathbf{x}, \mathbf{x}^i)}. \quad (2)$$

84 In this equation, $k = 4G\langle M_L \rangle(1+z_L)/c^3$, $M_{L,i}$ and \mathbf{x}^i refer to the mass and position of the i th microlens, respectively,
 85 and N_* indicates the number of microlenses. The parameters κ and γ denote the convergence and shear of the macro

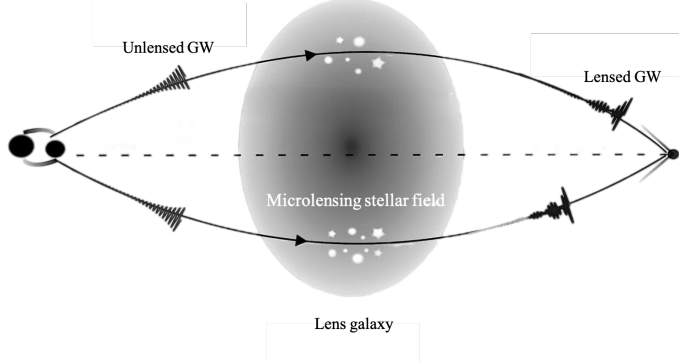


Figure 1. Illustrative sketch of a strong lensing gravitational wave (GW) influenced by a microlensing stellar field. A GW source is depicted on the far left. The signal propagating towards the lens galaxy (elliptical shape) represents the unlensed waveform. Individual stars within the lens galaxy act as microlenses. The signal emerging after passing through the lens galaxy is the lensed waveform, observed by a GW detector on the far right.

lens, respectively. Additionally, $t_{\text{smooth}}(\kappa, \gamma, \mathbf{x})$ and $t_{\text{micro}}(\mathbf{x}, \mathbf{x}^i)$ represent the macro and microlensing time delays, respectively. For simplicity, the macro image position is set to the origin ($\mathbf{y} = 0$). A negative mass sheet, represented by $\phi_-(\mathbf{x})$, is included to ensure that the total convergence κ remains unchanged when microlenses are added (Wambsganss 1990; Chen et al. 2021; Zheng et al. 2022).

Figure 1 shows an illustrative sketch of the strong lensing GW influenced by a microlensing stellar field in the lens galaxy. One can see that the strongly-lensed GW waveform is further modulated by the microlensing effect. Note that the number of stars depicted in the lens galaxy in this figure is purely illustrative and not intended to represent realistic values. Typically, the number of stars can range from 10^3 to 10^6 (Katz et al. 1986; Shan et al. 2023b).

In this study, we adopt the same strategy as in Shan et al. (2023a, 2024) to simulate the population of SLGW signals. Specifically, we assume that the merger rate of binary black holes is proportional to the star formation rate (Haris et al. 2018), and determine whether a GW event is a strong lensing event based on the multi-image optical depth of the singular isothermal sphere (SIS) model. We then calculate the microlensing stellar field density at the positions of the strong lensing images, which follow the Sérsic light profile (Vernardos 2018).

The microlensing stellar field consists of two components: stars and stellar remnants. Here, we assume that the stellar mass function follows the Chabrier initial mass function (Chabrier 2003), while the remnant mass function is determined using the initial-final mass relation described in Spera et al. (2015). Finally, we use the TAAH (Trapezoid Approximation-based Adaptive Hierarchical) method proposed by Shan et al. (2025) to evaluate the microlensing wave effects. For further details, please refer to Appendix A.

Based on the previous procedure, we will built two SLGW data sets: one containing events detectable at the O5 noise level, and the other containing events with the same GW waveform (the same strong and microlensing effects), but at a lower noise level (with the noise power spectrum reduced by a factor of 4 compared to O5). Each data set contains 125 binary black hole merger signals. The reason why we also choose a lower noise detector is that we want to investigate the influence of noise on the degeneracy and to see whether the precession evidence induced by microlensing could be a useful criterion for SLGWs in the future.

3. RESULT

3.1. Microlensing induced precession evidence

In this section, we characterize the degree of degeneracy between microlensing and precession by quantifying the precession Bayes factor induced by microlensing effects in SLGW signals. Specifically, the SLGW data generated in Section 2 do not include spin precession effects. However, in the parameter estimation procedure, we recover the GW parameters using the Dynesty (Higson et al. 2019) sampler and two different templates: IMRPhenomXP that includes precession effects, and IMRPhenomXAS that assumes parallel spins. We then compute the Bayes factor for the precession effect by comparing the detection evidences of the two templates.

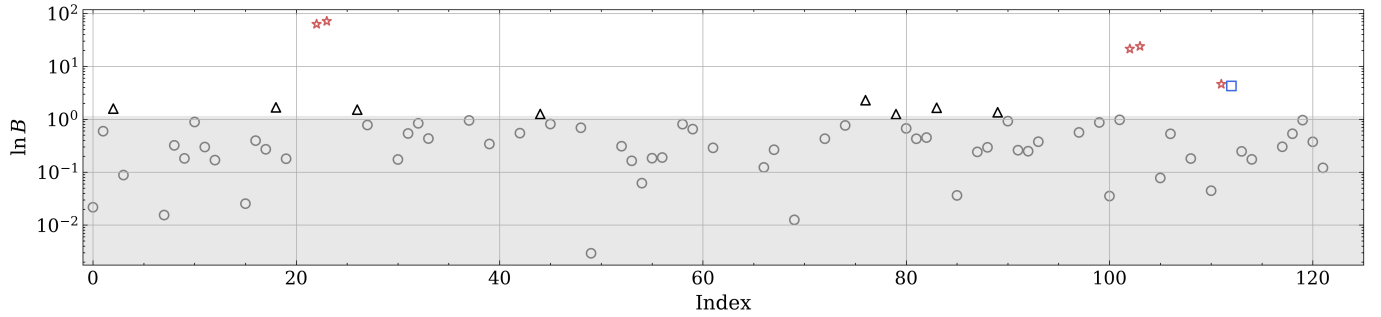


Figure 2. This figure shows the Bayes factor for microlensing-induced precession under O5 sensitivity. The gray circles within the shaded region represent events where the Bayes factor is less than 1.16, indicating insignificant evidence. Red stars indicate Bayes factors greater than 4.6, representing decisive evidence. Blue squares represent Bayes factors between 2.3 and 4.6, indicating strong evidence, while black triangles represent Bayes factors between 1.16 and 2.3, indicating substantial evidence. Only values with Bayes factors greater than 0 are shown.

Figure 2 shows the natural logarithm of the Bayes factor, $\ln B$, for 125 simulated SLGW events injected at the O5 noise level, where the x-axis represents the index of the SLGW events. Five events of the catalog, marked with red stars, have $\ln B$ greater than 4.6, indicating decisive evidence for precession (according to Jeffreys's scale (Jeffreys 1998)). One event, marked with a blue square, has $\ln B$ in the range of 2.3 to 4.6, corresponding to a strong evidence for precession. Additionally, eight events, marked with black triangles, have $\ln B$ in the range of 1.16 to 2.3, representing substantial evidence for precession. The remaining events, marked with grey circles under the shaded region, does not have statistically significant evidence to favour the precessing spin model. In summary, approximately 15% (14/125) of the SLGW events show non-negligible evidence of precession induced by microlensing wave-optical effects.

To further demonstrate that this precession-like effect is indeed caused by microlensing and that the events with $\ln B > 4.6$ reflects a degeneracy between the two factors, we analyze the time-domain waveform of one of the events with decisive evidence for precession, as shown in Figure 3. In this figure, the blue curve represents the reconstructed maximum likelihood waveform, while the orange curve is the original data, including noise. The top panel displays the result obtained using a template that includes precession, while the bottom panel shows the best waveform obtained using a template without precession. The legend in these two panels shows the match value between the reconstructed waveform and the injected signal. One can see that the waveform incorporating precession provides a better fit to the data. This suggests that there is indeed some degeneracy between microlensing and precession effects, leading to favorable evidence for precession.

Next, we apply the same method to analyze the second simulated data set assuming a more sensitive detector configuration. In this dataset, the SLGW waveform remains consistent with the previous dataset; however, the noise power spectrum exhibits a four-fold reduction, leading to a two-fold enhancement in the SNR.

The results are shown in Figure 4. One can see that more events show detectable “precession” effects mimicking the microlensing wave-optical effects. There are 17, 9, and 11 events showing decisive, strong, and substantial evidence for precession, respectively. Overall, 30% of the SLGW events demonstrate non-negligible evidence for precession. This result is intuitive, as the waveform modulation caused by microlensing is easier to detect under a lower noise level. It is also easier to distinguish precessional and non-precessional events with better signal SNR. Therefore, one can anticipate that precession will become an even more common feature of SLGW detections, especially in the upcoming third-generation (3G) era.

Coincidentally, one can see that the precession detection rate compared to the O5 sensitivity level (15%) is roughly proportional to the SNR boost (a factor of 2). Therefore, for 3G detectors, such as Cosmic Explorer (CE) and Einstein Telescope (ET), it is reasonable to expect that almost all microlensing-induced precession will be detected, as the SNR can achieve approximately a tenfold increase compared to O5 sensitivity.

Although the precessional waveform can mimic some of the microlensing features, it can not describe and fully match the waveform. It means that for these high SNR event, if we use precessional waveform to fit the microlensing event, the residual might be exceptionally large given the detector noise level. This may be one way to distinguish the precessional systems from the micro-lensed system even if we don't have/use the microlensing waveform for PE.

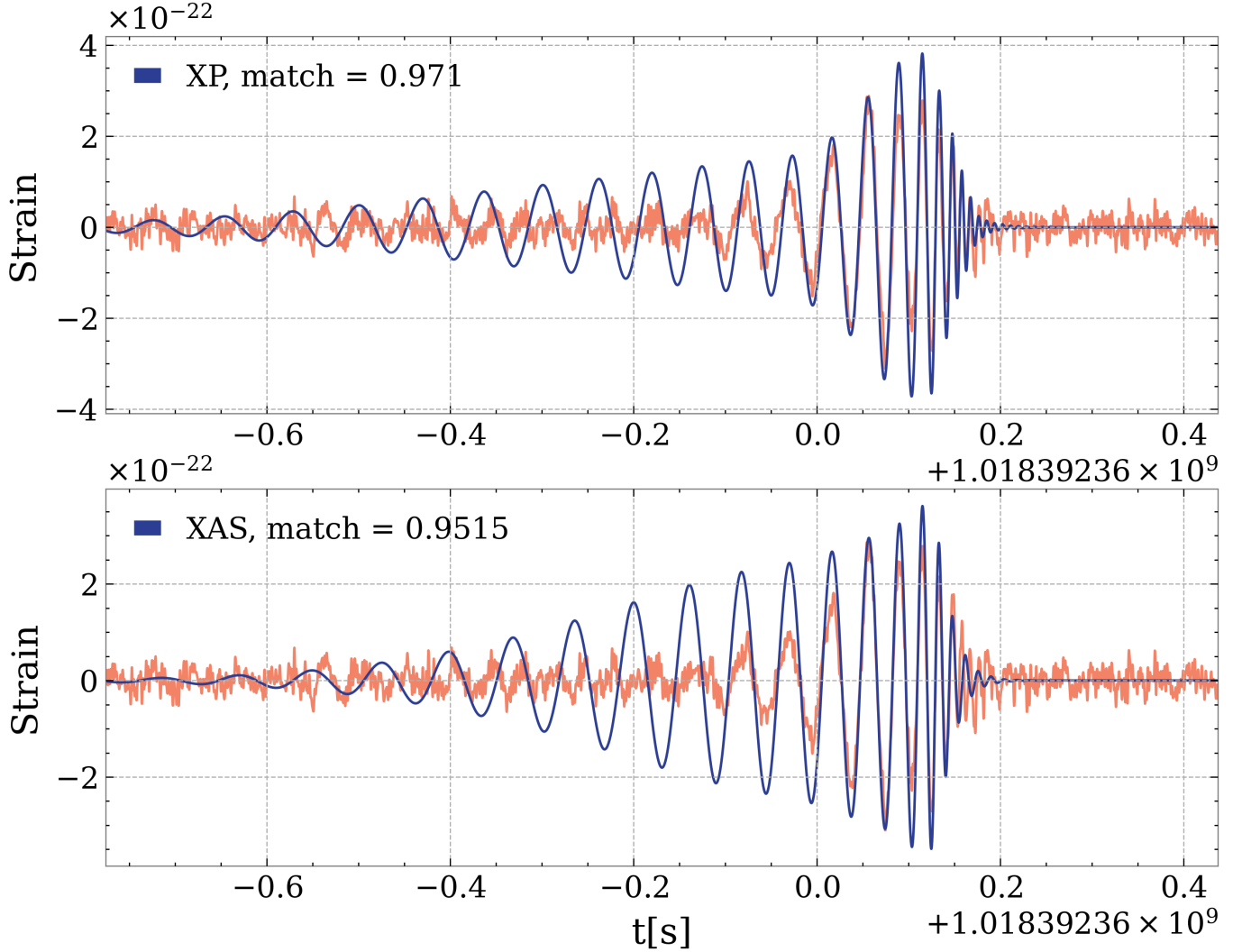


Figure 3. Comparison between the reconstructed signal (blue curve) and the data (orange curve) for an example with a $\ln B$ greater than 4.6, using different templates. The top panel shows the result obtained using a precession template (IMRPhenomXP), while the bottom panel presents the result obtained without considering precession (IMRPhenomXAS). The numbers indicate the match value between the reconstructed waveform and the injected signal. This comparison demonstrates that the precession template can partially capture the microlensing-induced oscillation effect (around 0 s on the x-axis), leading to detectable evidence for precession.

Based on the above findings, we conclude that the microlensing-induced precession is more pronounced as the detector noise decreases. Therefore, the frequent presence of precession could be used as a discriminative factor to constrain false SLGW candidates for future detectors.

3.2. Precession false alarm event

Aside from microlensing-induced precession measurements, one might also wonder whether other effects could influence precession measurements, such as false precession signals induced by noise. For this reason, this section will investigate false alarm precession events arising from noise within the data. To achieve this, we simulate 125 standard GW events (i.e., events that are neither strongly lensed nor exhibit any precession effects) under O5 sensitivity, alongside 125 additional common GWs with their SNR boosted by a factor of two.

Figure 5 illustrates the events that exhibit decisive precession evidence ($\ln B > 4.6$) among these 250 standard GW events and 250 strongly lensed GWs (SLGWs). The blue and red stars represent the standard GWs and SLGWs, respectively. The x-axis denotes the signal-to-noise ratio (SNR) of the GW, while the y-axis indicates the chirp mass.

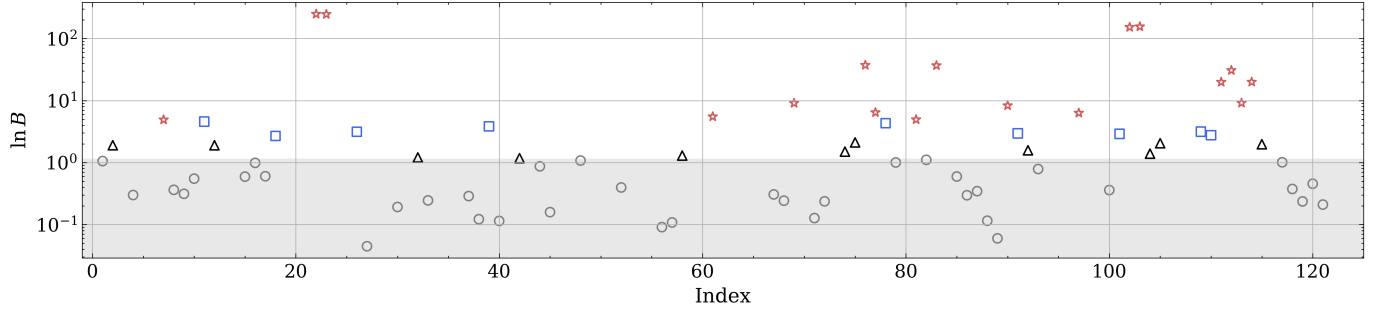


Figure 4. Similar to the results shown in Figure 2, but using a more sensitive detector configuration.

Notably, some standard events (22 out of 250) exhibit precession signatures purely due to noise present in the GW data. These events can be categorized as false alarms in the analysis of microlensing-induced precession effects.

However, by comparing the two datasets, we observe that all standard events with decisive precession evidence have a chirp mass below 35 solar masses (based on current population model) and exhibit a relatively lower SNR, whereas the strongly lensed events can have a chirp mass exceeding 35 solar masses with a higher SNR. This distinction arises because lower chirp mass events evolve more slowly, resulting in longer signal durations compared to those with higher chirp masses. This relationship can be understood more clearly with the following equation:

$$\dot{f} = \frac{96}{5} \pi^{8/3} \left(\frac{GM}{c^3} \right)^{5/3} f^{11/3}, \quad (3)$$

where $\dot{f} = \frac{df}{dt}$ represents the time derivative of the GW frequency, indicating its rate of change over time, and M is the chirp mass of the binary black hole system.

Long-duration signals with lower SNR are more susceptible to periodic modulation effects from noise at lower frequencies, where the precession effect is easier to detect. This susceptibility explains why false alarm events tend to have lower chirp masses and lower SNRs statistically.

Figure 6 provides an example of an event with decisive precession evidence that is purely induced by noise. The top panel displays the result obtained using a precession template, while the bottom panel shows the result without accounting for precession. The blue and orange curves represent the reconstructed maximum likelihood signal and the original data, respectively. One can see that the precession modulation better aligns with a long-period noise fluctuation.

Based on these results, we conclude that for a event identified with detectable precession, a higher chirp mass and a higher SNR correspond to a lower probability of a false alarm caused by noise.

3.3. Test high magnification events

One possible explanation for GW events residing in the mass gap is that they are highly magnified by the strong lensing galaxy (Broadhurst et al. 2018, 2020; Broadhurst et al. 2020), such as GW190425 (Abbott et al. 2020), GW190426_152155 (Abbott et al. 2021a), GW190521 (Abbott et al. 2020) and GW230529 (Abac et al. 2024). To align with stellar evolution theory, such events would require strong lensing magnifications ranging from 10 to even 1000 (Pang et al. 2020; Abbott et al. 2021b), which effectively lowers the observed source mass in the source frame, given by $m_s = m_{\text{obs}}/(1+z)$. However, strong lensing magnification can also enhance the effective microlens mass by a factor of μ , which, in turn, leads to a more significant wave-optical effect.

In this section, we simulate a subset (22 events) of highly magnified, strongly lensed events with magnifications around 100 to investigate whether precession measurements could serve as additional evidence for extreme lensing.

The results are presented in Figure 7. The gray circles represent events where the Bayes factor is less than 1.16, indicating evidence barely worth mentioning. Red stars indicate Bayes factors greater than 4.6, representing decisive evidence, while blue squares represent Bayes factors between 2.3 and 4.6, indicating strong evidence. The dashed horizontal line in this figure is the same as the line in Figure 5, which indicates the highest chirp mass of events, in the simulation data set, with precession induced by noise.

To mitigate the influence of such noise-induced false alarms, we focus our analysis on the subset of events with chirp masses above 35 solar masses, which comprises 11 of the 22 simulated events. We can see that 8/11, i.e., $\sim 72\%$ of these

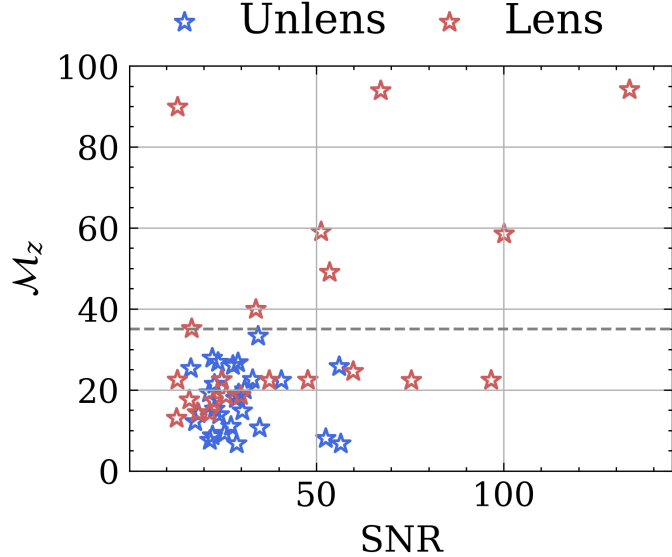


Figure 5. Signal-to-noise ratio (SNR) and chirp mass for GW events with decisive precession evidence ($\ln B > 4.6$). Blue stars denote common GW events (neither strongly lensed nor exhibiting precession effects in the injected waveforms), while red stars represent SLGW events.

events, show at least strong evidence for precession. Thus, for highly magnified events (with chirp mass $> 35 M_{\odot}$), microlensing-induced precession may serve as a characterization tool to further ascertain whether an event is a highly magnified candidate.

3.4. Correlation between microlensing and precession

The preceding results indicate a degeneracy between microlensing and precession. Testing whether larger values of the precession evidence, $\ln B$, indicate a stronger microlensing signature is crucial. This knowledge would allow us to infer microlensing strength from $\ln B$. To this end, in this section, we investigate the correlation between the strength of microlensing and the precession evidence $\ln B$. Here, we use the mismatch in the GW waveform induced by microlensing to quantify the microlensing strength. The mismatch is defined as follows:

$$\text{mismatch} = 1 - \max_{\phi_0, t_0} \frac{\langle h_1 | h_2 \rangle}{\sqrt{\langle h_1 | h_1 \rangle \langle h_2 | h_2 \rangle}}, \quad (4)$$

where h_1 and h_2 represent the waveforms of signals 1 and 2, respectively. ϕ_0 and t_0 are the initial phase and start time of signal 1. This equation accounts for the time delays caused by both macrolensing and microlensing. The operator $\langle \cdot | \cdot \rangle$ represents the noise-weighted inner product, defined as:

$$\langle h_1 | h_2 \rangle = 4 \text{Re} \int_{f_{\text{low}}}^{f_{\text{high}}} df \frac{h_1^*(f) h_2(f)}{S_n(f)}, \quad (5)$$

where $S_n(f)$ is the single-sided power spectral density of the detector noise, and “ $*$ ” denotes the complex conjugate. In this analysis, signal 1 represents the unlensed waveform h_U , while signal 2 represents the macro and micro lensed waveform h_L .

To quantify the correlation between microlensing and precession, we used Spearman’s correlation coefficient. Specifically, we aimed to determine whether stronger microlensing effects generally lead to higher evidence for precession, or conversely, whether higher evidence for precession corresponds to a stronger microlensing effect. Figure 8 shows the $\ln B$ distribution of SLGW events as a function of microlensing mismatch. The left panel shows the events under O5 sensitivity, while the right panel shows the events with SNR boosted by a factor of 2, here referred to as O5 plus. In this analysis, we calculate the correlation between microlensing and precession using two different datasets.

First, we use the complete dataset to determine if stronger microlensing effects generally lead to higher evidence for precession. Second, we use a subset containing only events with a Bayes factor $\ln B > 0$, which indicates positive

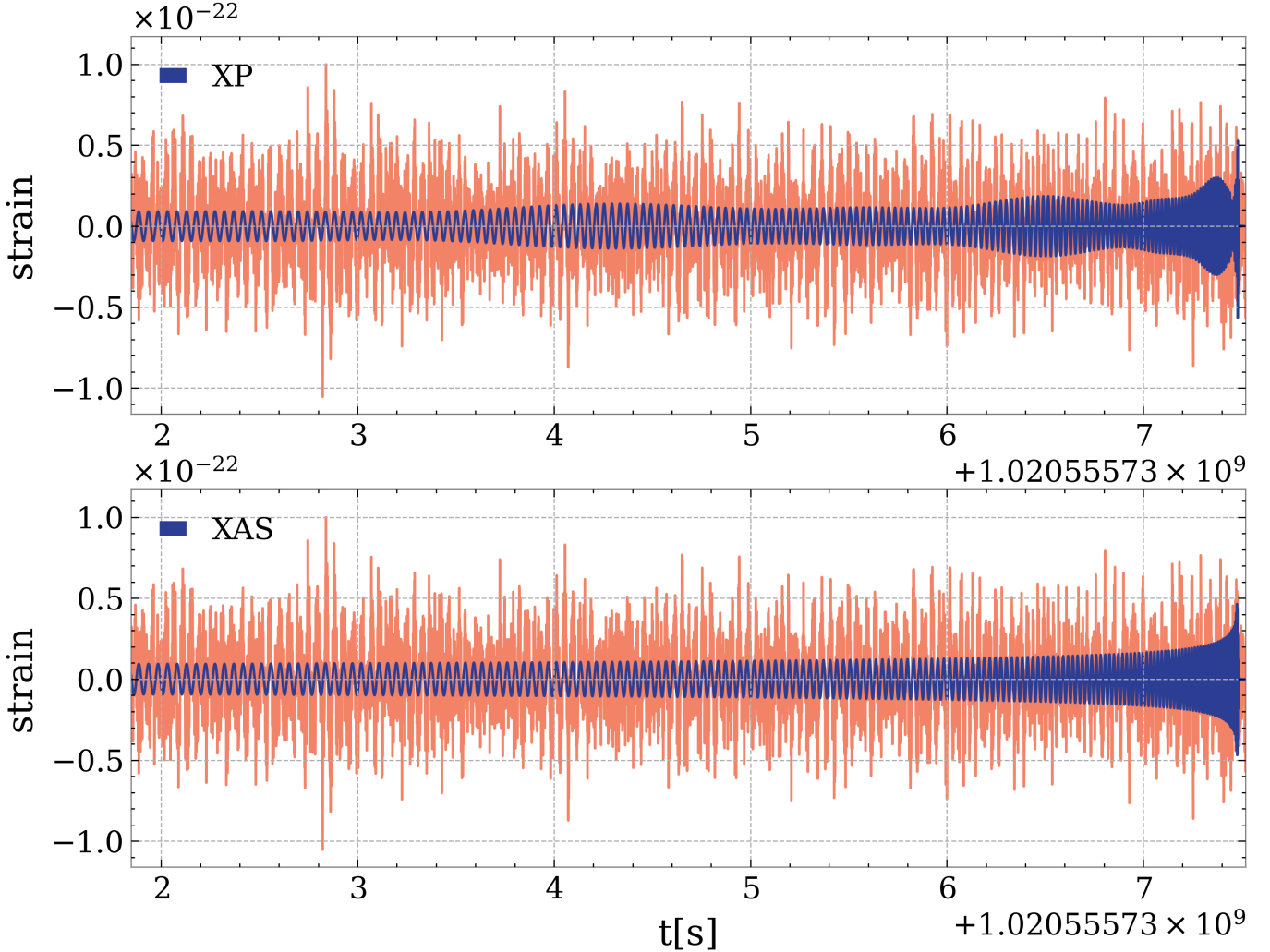


Figure 6. Comparison between the reconstructed signal (blue curve) and data (orange curve) for a common GW event (i.e., an event that is not strongly lensed and has no precession effect in the injected waveform) with $\ln B > 4.6$, using different templates. The top panel shows the result obtained using a precession template (IMRPhenomXP), while the bottom panel presents the result obtained without considering precession (IMRPhenomXAS).

evidence of precession. This second dataset allows us to investigate the converse question: whether higher evidence for precession corresponds to a stronger microlensing effect. The rationale for using this second, filtered dataset is that evidence for precession is an observable quantity. We want to determine if stronger observational evidence for it implies a more significant microlensing effect. The correlation coefficient r and P value for these two scenarios are shown in the legend, distinguished by the colors grey and blue.

To minimize the influence of false positives from detector noise effects (discussed in Section 3.2), we restrict our analysis to events with a chirp mass greater than 35 solar masses.

One can see that for the complete dataset, the correlation between microlensing and precession is weak for both O5 and O5 plus sensitivities. Therefore, regarding the first question—whether a stronger microlensing effect corresponds to higher evidence of precession—the answer is that the correlation is weak. For the O5 plus sensitivity, we can reject the null hypothesis of “no correlation” at a significance level of 2×10^{-2} .

However, for the selected dataset, which includes only events with $\ln B > 0$, both the correlation coefficient and the P value are higher compared to the complete dataset. Specifically, for the O5 plus sensitivity, the correlation coefficient increases to 0.43, and the P value decreases to approximately 0.001.

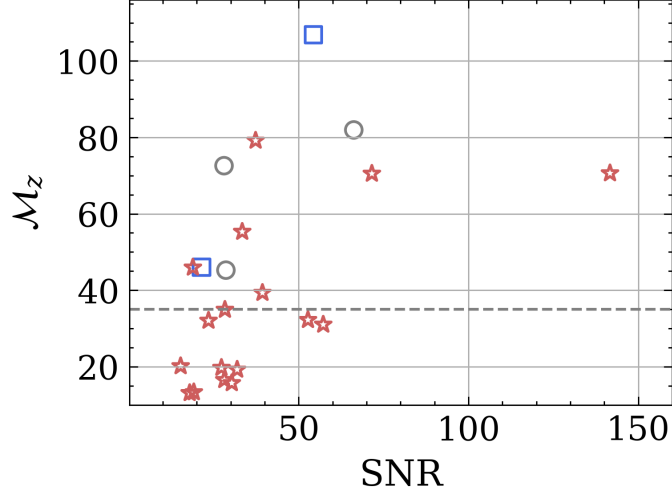


Figure 7. Signal to noise ratio (SNR) and chirp mass for highly magnified ($\mu \simeq 100$) GW events. The gray circles represent events where the Bayes factor is less than 1.16, indicating evidence barely worth mentioning. Red stars indicate Bayes factors greater than 4.6, representing decisive evidence. Blue squares represent Bayes factors between 2.3 and 4.6, indicating strong evidence.

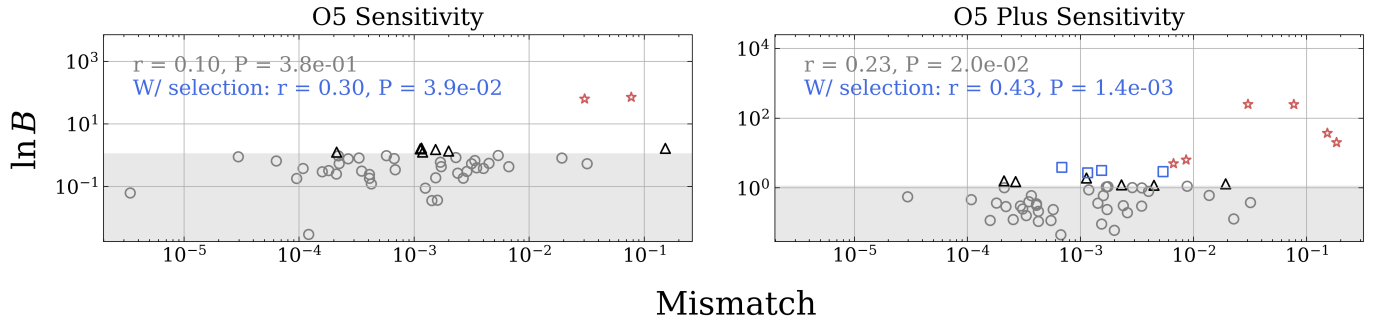


Figure 8. Correlation (Spearman correlation coefficient) between the Bayes factor and microlensing mismatch for events with chirp mass greater than 35. The left panel shows the O5 sensitivity, while the right panel shows the O5 plus sensitivity. Red stars indicate a Bayes factor greater than 4.6, blue square markers indicate a Bayes factor between 2.3 and 4.6, and black triangles indicate a Bayes factor between 1.16 and 2.3. In the legend, grey indicates the correlation coefficient (r) and P value for the complete dataset, while blue represents the results for events with $\ln B > 0$.

Therefore, at the 0.001 significance level, we can confidently conclude that there is a moderate positive correlation between the precession evidence and the strength of the microlensing effect. This suggests that for events with $\ln B > 0$, stronger evidence of precession may imply a more significant microlensing effect.

Finally, we have investigated the correlation between microlensing strength and precession evidence for two types of SLGW images: Type I, originating from the minimum point of the time delay surface, and Type II, originating from the saddle point of the time delay surface. In this analysis, we only consider events under O5 plus sensitivity (shown in the right panel of Figure 8) and 10 high-magnification events (evenly divided between Type I and Type II images), as described in Section 3.3. The results are shown in Figure 9.

The left panel of the figure corresponds to Type I images, while the right panel shows Type II images. Here, we also restrict our analysis to events with chirp masses greater than 35 solar masses to reduce the impact of false positives caused by noise effects.

One can find that the correlation for Type II images appears to be stronger than for Type I images, a trend observed in both the complete dataset (grey in the legend) and the subset of events with $\ln B > 0$ (blue in the legend).

For the complete dataset, the correlation coefficients for Type I and Type II images are 0.34 and 0.55, respectively. Both image types yield P values of approximately 10^{-3} , demonstrating statistical significance at this level. Therefore, we can conclude that for each strong lensing image type, there is a weak to moderate positive correlation between the

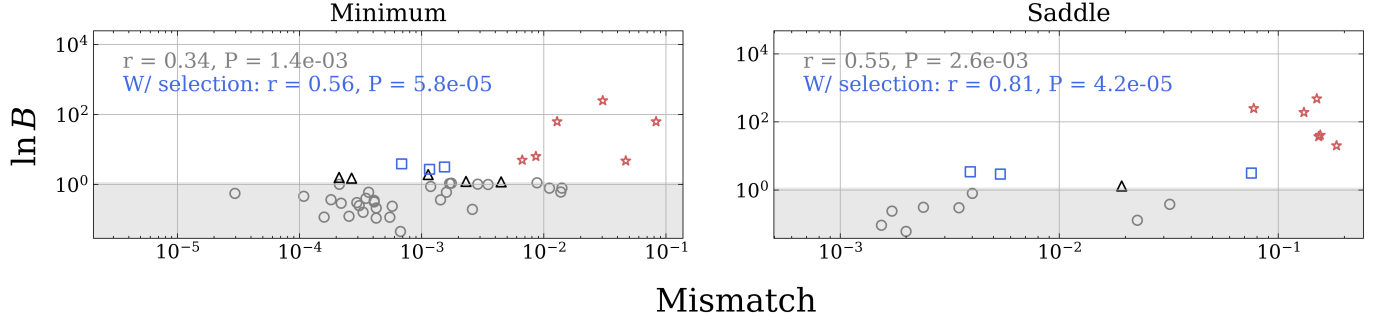


Figure 9. Correlation (Spearman correlation coefficient) between Bayes factor and microlensing mismatch for different types of strong lensing images. The left panel shows the Minimum point, while the right panel shows the Saddle point. Red stars indicate a Bayes factor greater than 4.6, blue square markers indicate a Bayes factor between 2.3 and 4.6, and black triangles indicate a Bayes factor between 1.16 and 2.3. In the legend, grey indicates the correlation coefficient (r) and P value for the complete dataset, while blue represents the results for events with a Bayes factor of $\ln B > 0$. It is observed that the correlation between microlensing and Bayes factor is stronger for the Saddle point, suggesting that microlensing at Saddle points is more likely to mimic precession effects.

strength of the microlensing effect and the evidence for precession. Thus, one can expect to observe stronger evidence for precession when the microlensing effect is more significant.

The correlation appears stronger when the data is separated by image type, as presented here, compared to the combined analysis in Figure 8. This is because the strength of the correlation differs between Type I and Type II images.

For the sub-dataset of events with $\ln B > 0$, the correlation is even stronger, with coefficients of 0.56 for Type I and 0.81 for Type II images, respectively. Both results yield P values of approximately 5×10^{-5} , indicating a high degree of statistical significance. Given these strong correlation coefficients and extremely low P values, one can confidently conclude that for events already showing evidence of precession ($\ln B > 0$), stronger evidence for precession corresponds to a more significant microlensing effect.

Finally, it is noteworthy that in both datasets (the complete set and the $\ln B > 0$ subset), the correlation between precession and the microlensing effect is consistently stronger for Type II images than for Type I images.

These results suggest that microlensing effects in Type II images more easily mimic precession effects. This is likely because the microlensing effects in these images exert a more pronounced modulation on the phase. The phase modulation between Type I and Type II can be compared in the rightmost panel of Figure 10, as clearly shown there. Therefore, for one SLGW pair, one may expect to observe one event with a precession effect and another without a precession effect. Consequently, in the identification of SLGW using the parameter overlapping method or joint parameter estimation method, we need to carefully treat these precession parameters.

4. CONCLUSION AND DISCUSSION

The wave-optical effect in gravitational lensing can induce frequency-dependent fluctuations in gravitational wave (GW) waveforms, often referred to as a “beat pattern” (Hou et al. 2020). In addition to the beat pattern caused by lensing, intrinsic physical characteristics, such as precession effects due to misaligned spins in binary black hole (BBH) sources, can also produce similar beat patterns.

Liu & Kim (2024) demonstrated that these two types of beat patterns can be distinguished using an MCMC-based method, which involves creating a template that includes both the lensing effect and spin-induced precession. However, their approach is feasible under specific conditions, such as the millilensing scenario, where only nearby massive objects ($M > 10^2, M_\odot$) need to be considered. In this scenario, the number of such objects is sufficiently small to make template construction manageable.

In contrast, the stellar microlensing field contains many objects, and the number of stars and remnants that need to be accounted for can be as high as 10^6 (Katz et al. 1986). Consequently, building a comprehensive template in this context is challenging. Therefore, distinguishing between microlensing-induced beat patterns and intrinsic precession using a template-based method becomes difficult.

In this work, we have investigated the probability of precession-like features induced by microlensing wave effects caused by a stellar-mass microlensing field embedded within a strongly lensing galaxy, and the correlation between

precession evidence and microlensing wave effects. We simulated two SLGW datasets observed by two detector networks (LIGO-Virgo-like) with different noise sensitivity curves. One dataset is generated under O5 noise conditions, while the other assumes a noise power spectrum reduced by a factor of four, which we refer to as O5 plus for simplicity.

Figure 2 shows the precession ln Bayes factor for SLGWs under O5 sensitivity. One can see that, approximately 15% of the simulated SLGW events exhibits substantial evidence for precession, with about 4% showing decisive evidence (Bayes factor $\ln B > 4.6$). This suggests that microlensing wave-optical effects in SLGW can indeed mimic precession phenomena.

We further demonstrate that this effect becomes even more pronounced with improved detector sensitivity. Figure 4 shows the results using a more sensitive detector. One can see that the proportion of SLGW events showing at least “substantial” precession evidence increased to 30%. Compared to the O5 sensitivity, this represents an increase by a factor of 2, consistent with the enhancement in the SNR. These findings suggest that as detector sensitivity improves, microlensing-induced precession features become more detectable.

This result suggests that precession signature may serve as distinctive feature of SLGW event, potentially providing supplementary evidence for its identification. This will be particularly valuable for third-generation (3G) detectors, where the signal-to-noise ratio (SNR) could be enhanced by up to a factor of 10 compared to O5 detectors. By extrapolating the observed relationship between O5 plus and O5, one can anticipate that the proportion of SLGW events exhibiting “substantial” precession evidence could reach nearly $\sim 100\%$ with 3G detectors. Moreover, although the precessional waveform mimics some microlensing features, it fails to fully describe or match the waveform. For high-SNR events, this mismatch means fitting with a precessional model will likely produce residuals exceeding detector noise expectations. This discrepancy offers a way to distinguish precessional from microlensed systems, even in the absence of a microlensing waveform template for PE.

In this study, we have also explored the occurrence of false-positive precession events due to noise, the results are shown in Figure 5. We find that common GW events (i.e., not strongly lensed and without intrinsic precession signals) with lower chirp masses and lower SNR were more susceptible to false positives, due to their longer and weaker waveform, which makes them more easily influenced by long-periodic noise fluctuations. Therefore, for events with higher chirp mass and SNR, the detection of significant precession evidence indicates a higher probability of corresponding to a genuine precession-like effect, whether originating from intrinsic precession or as a mimicker of microlensing phenomena.

In addition, we investigated the correlation between the strength of the microlensing effect and the evidence for precession. We analyzed this correlation assuming two different detector noise levels, with the results presented in Figure 8.

We found that the overall correlation between the microlensing effect and precession evidence is weak, though it increases as detector sensitivity improves. However, when considering a subset of events with existing evidence for precession ($\ln B > 0$), the correlation between these two quantities is significantly enhanced, particularly for the O5 plus sensitivity. For this subset, the correlation coefficient is 0.43, and the P value of approximately 0.001 allows us to reject the null hypothesis—that “there is no correlation between precession and microlensing effects”—at the 0.001 significance level. This result implies that stronger evidence for precession may indicate a more significant microlensing effect.

Finally, we have examined the correlation for two different types of SLGW images—those originating from the minimum point of the time delay surface (Type I) and those from the saddle point (Type II). The results indicate that microlensing effects in Type II images are more likely to mimic precession evidence, exhibiting stronger correlation coefficients compared to Type I images. This is likely because microlensing effects exert a more pronounced modulation on the phase of Type II images, making them more susceptible to being misinterpreted as precession.

In conclusion, the findings of this study emphasize the need for caution when interpreting precession evidence in GW detections. Significant evidence for precession may not only indicate genuine precession, suggesting that the binary black hole (BBH) originated from a dynamical channel, but could also be interpreted as an SLGW event influenced by microlensing wave effects. Due to the fact that, among the approximately 100 GW events currently cataloged, only GW200129 (Hannam et al. 2022) exhibits evidence of precession, the observed precession rate in the standard GW dataset is only 1%. Therefore, in certain cases, precession can serve as supplementary evidence for SLGW, particularly in high-magnification events. This also means that those GW events that fall within the mass gap and exhibit significant precession effects are also consistent with the scenario of being high-magnification SLGW events.

342 This work is partly supported by the National Science Foundation of China (Grant No. 12133005). X.S. acknowledges
 343 support from Shuimu Tsinghua Scholar Program (No. 2024SM199).

APPENDIX

A. SIMULATION PROCEDURES

346 Complementing Section 2, this appendix details the simulation procedures used to generate a mock dataset. Using
 347 the Monte Carlo method and following the procedure described in Haris et al. (2018); Xu et al. (2022); Shan et al.
 348 (2024), we synthesized a population of gravitational wave events. The key simulation steps were:

349 **Source Redshift Determination:** Redshifts (z_s) for the sBBH population were drawn from a distribution derived
 350 from a theoretical merger rate model. This model assumes the merger rate tracks the star formation history, offset by
 351 a characteristic delay time ($\Delta t = 50\text{Myr}$) between stellar birth and binary coalescence.

352 **Source Parameterization:** Intrinsic (masses m_1, m_2 ; spins a_1, a_2) and extrinsic (position α, δ ; orientation ι, ψ ; time
 353 t_c) parameters were assigned based on astrophysically motivated distributions (e.g., peaked power-law for masses (Abbott et al. 2019), sine distribution for ι , uniform for others).

355 **Strong Lensing Selection:** The likelihood of an sBBH at redshift z_s undergoing strong lensing (multiple imaging)
 356 was evaluated using the SIS optical depth, $\tau(z_s)$ (Haris et al. 2018). A stochastic selection was performed: if $\tau(z_s)$
 357 exceeded a random variate drawn from $U(0, 1)$, the event was flagged as an SLGW; otherwise, it was discarded.

358 **Lens Modeling for SLGWs:** Lensing effects for candidates were computed using an SIE model (Kormann et al.
 359 1994), with lens properties (σ_v, q) drawn from SDSS galaxy survey statistics (Choi et al. 2007; Wierda et al. 2021).

360 **Observational Filtering:** Detectability was assessed using a three-detector network (LIGO Livingston/Hanford,
 361 Virgo) and an SNR threshold of 12. The simulation proceeded until 125 detectable SLGW events were obtained.

362 **Microlensing Environment Simulation:** The final stage involved modeling the microlensing environment pertinent
 363 to each detected SLGW. This included defining a stellar mass function based on the Chabrier IMF (Chabrier 2003)
 364 for stars in the mass range $[0.1, 1.5]M_\odot$ (Diego et al. 2022), and assuming an elliptical Sérsic profile (Vernardos 2018)
 365 for their density. A population of remnant objects was also incorporated, using an initial-final mass relation (Spera
 366 et al. 2015) for their masses and assuming their mass density constitutes 10% of the stellar mass density.

367 Figure 10 presents the microlensing diffraction results for these simulated SLGW events. Different curves represent
 368 different events. The first and second rows illustrate results for Type I and Type II SLGWs, respectively. The first
 369 column shows the residual time-domain amplification factor ($F(t) - F_{\text{smooth}}(t)$, where $F_{\text{smooth}}(t)$ excludes microlensing
 370 effects). The second and third columns display the normalized frequency-domain amplification factor and the complex
 371 phase. The gradual convergence of each curve's tail towards zero in the first column indicates the convergence of the
 372 diffraction integral (Shan et al. 2023b).

REFERENCES

- 373 Abac, A. G., Abbott, R., Abouelfettouh, I., et al. 2024,
 374 ApJL, 970, L34, doi: [10.3847/2041-8213/ad5beb](https://doi.org/10.3847/2041-8213/ad5beb)
- 375 Abbott, B. P., et al. 2016, Phys. Rev. Lett., 116, 061102,
 376 doi: [10.1103/PhysRevLett.116.061102](https://doi.org/10.1103/PhysRevLett.116.061102)
- 377 Abbott, B. P., Abbott, R., Abbott, T. D., et al. 2019,
 378 ApJL, 882, L24, doi: [10.3847/2041-8213/ab3800](https://doi.org/10.3847/2041-8213/ab3800)
- 379 Abbott, B. P., Abbott, R., Abbott, T. D., et al. 2020, The
 380 Astrophysical Journal Letters, 892, L3,
 381 doi: [10.3847/2041-8213/ab75f5](https://doi.org/10.3847/2041-8213/ab75f5)
- 382 Abbott, R., Abbott, T. D., Abraham, S., et al. 2020, ApJL,
 383 900, L13, doi: [10.3847/2041-8213/aba493](https://doi.org/10.3847/2041-8213/aba493)
- 384 Abbott, R., et al. 2021a, Phys. Rev. X, 11, 021053,
 385 doi: [10.1103/PhysRevX.11.021053](https://doi.org/10.1103/PhysRevX.11.021053)
- 386 Abbott, R., Abbott, T. D., Abraham, S., et al. 2021b, The
 387 Astrophysical Journal, 923, 14,
 388 doi: [10.3847/1538-4357/ac23db](https://doi.org/10.3847/1538-4357/ac23db)
- 389 Belczynski, K., Holz, D. E., Bulik, T., & O'Shaughnessy, R.
 390 2016, Nature, 534, 512–515, doi: [10.1038/nature18322](https://doi.org/10.1038/nature18322)
- 391 Broadhurst, T., Diego, J. M., & Smoot, III, G. 2018, arXiv
 392 e-prints, arXiv:1802.05273,
 393 doi: [10.48550/arXiv.1802.05273](https://doi.org/10.48550/arXiv.1802.05273)

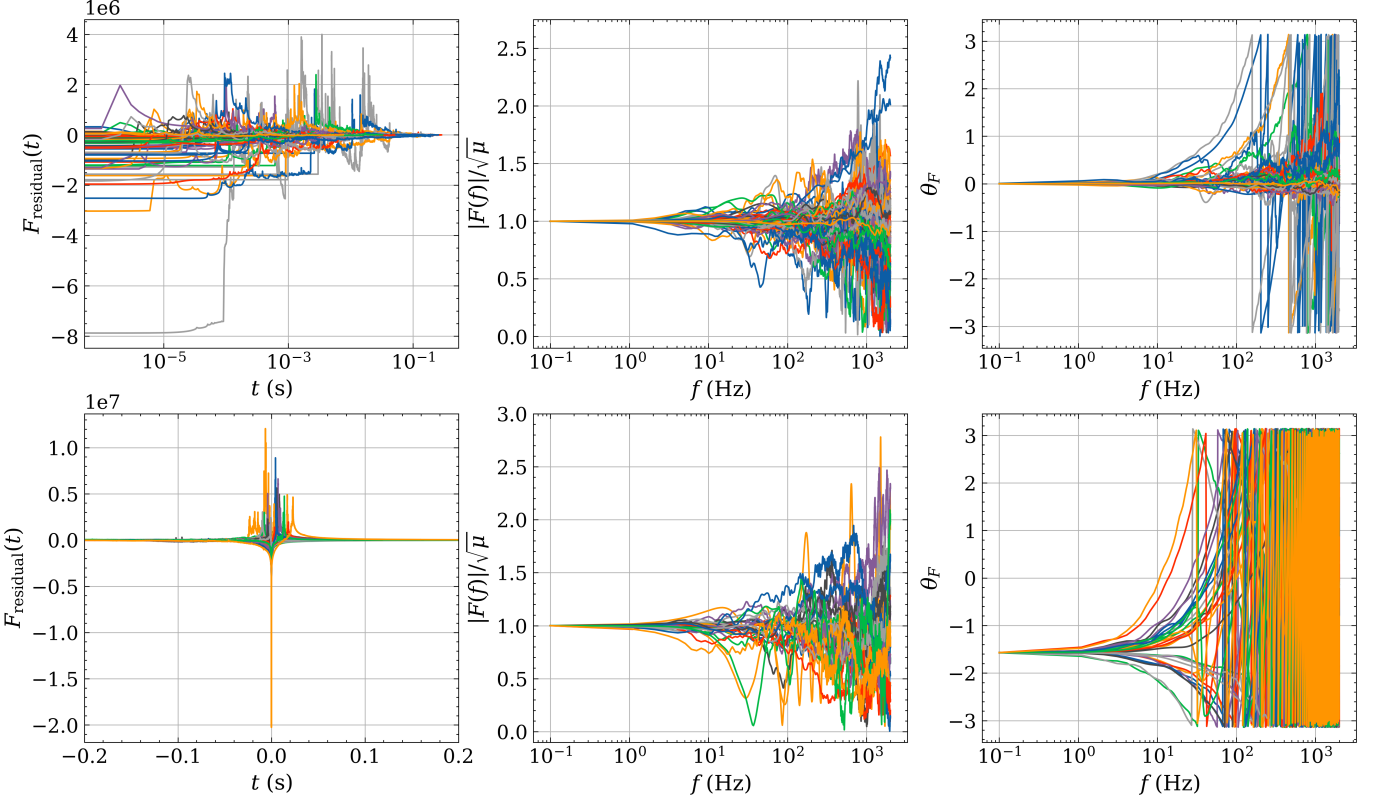


Figure 10. Microlensing diffraction results for 125 strongly lensed gravitational wave (SLGW) events observed by a LIGO-Virgo detector network. Each curve corresponds to a different event. The first and second rows depict the results for Type I and Type II SLGWs, respectively. The first, second, and third columns display the residual time-domain amplification factor ($F(t) - F_{\text{smooth}}(t)$, where $F_{\text{smooth}}(t)$ excludes microlensing effects), the normalized frequency-domain amplification factor, and the complex phase, respectively.

- 394 Broadhurst, T., Diego, J. M., & Smoot, G. F. 2020, arXiv
 395 e-prints, arXiv:2002.08821,
 396 doi: [10.48550/arXiv.2002.08821](https://doi.org/10.48550/arXiv.2002.08821)
- 397 Broadhurst, T., Diego, J. M., & Smoot, G. F. 2020.
 398 <https://arxiv.org/abs/2006.13219>
- 399 Chabrier, G. 2003, PASP, 115, 763, doi: [10.1086/376392](https://doi.org/10.1086/376392)
- 400 Chen, X., Shu, Y., Li, G., & Zheng, W. 2021, The
 401 Astrophysical Journal, 923, 117,
 402 doi: [10.3847/1538-4357/ac2c76](https://doi.org/10.3847/1538-4357/ac2c76)
- 403 Choi, Y., Park, C., & Vogeley, M. S. 2007, The
 404 Astrophysical Journal, 658, 884–897, doi: [10.1086/511060](https://doi.org/10.1086/511060)
- 405 Diego, J. M., Bernstein, G., Chen, W., et al. 2022, Astron.
 406 Astrophys., 662, A34, doi: [10.1051/0004-6361/202143009](https://doi.org/10.1051/0004-6361/202143009)
- 407 Diego, J. M., Hannuksela, O. A., Kelly, P. L., et al. 2019,
 408 Astron. Astrophys., 627, A130,
 409 doi: [10.1051/0004-6361/201935490](https://doi.org/10.1051/0004-6361/201935490)
- 410 Giacobbo, N., & Mapelli, M. 2018, MNRAS, 480, 2011,
 411 doi: [10.1093/mnras/sty1999](https://doi.org/10.1093/mnras/sty1999)
- 412 Hannam, M., Hoy, C., Thompson, J. E., et al. 2022,
 413 Nature, 610, 652, doi: [10.1038/s41586-022-05212-z](https://doi.org/10.1038/s41586-022-05212-z)
- 414 Hannuksela, O. A., Collett, T. E., Çahışkan, M., & Li, T.
 415 G. F. 2020, Mon. Not. Roy. Astron. Soc., 498, 3395,
 416 doi: [10.1093/mnras/staa2577](https://doi.org/10.1093/mnras/staa2577)
- 417 Haris, K., Mehta, A. K., Kumar, S., Venumadhav, T., &
 418 Ajith, P. 2018. <https://arxiv.org/abs/1807.07062>
- 419 Higson, E., Handley, W., Hobson, M., & Lasenby, A. 2019,
 420 Statistics and Computing, 29, 891,
 421 doi: [10.1007/s11222-018-9844-0](https://doi.org/10.1007/s11222-018-9844-0)
- 422 Hou, S., Fan, X.-L., Liao, K., & Zhu, Z.-H. 2020, Phys.
 423 Rev. D, 101, 064011, doi: [10.1103/PhysRevD.101.064011](https://doi.org/10.1103/PhysRevD.101.064011)
- 424 Janquart, J., Seo, E., Hannuksela, O. A., Li, T. G. F., &
 425 Broeck, C. V. D. 2021, Astrophys. J. Lett., 923, L1,
 426 doi: [10.3847/2041-8213/ac3bcf](https://doi.org/10.3847/2041-8213/ac3bcf)
- 427 Jeffreys, H. 1998, Theory of Probability, International series
 428 of monographs on physics (Clarendon Press). https://books.google.com.tw/books?id=_PuRmAEACAAJ
- 429 Katz, N., Balbus, S., & Paczynski, B. 1986, ApJ, 306, 2,
 430 doi: [10.1086/164313](https://doi.org/10.1086/164313)
- 431 Kormann, R., Schneider, P., & Bartelmann, M. 1994, A&A,
 432 284, 285

- 434 Lai, K.-H., Hannuksela, O. A., Herrera-Martín, A., et al.
 435 2018, Phys. Rev. D, 98, 083005,
 436 doi: [10.1103/PhysRevD.98.083005](https://doi.org/10.1103/PhysRevD.98.083005)
- 437 Li, S.-S., Mao, S., Zhao, Y., & Lu, Y. 2018, Mon. Not. Roy.
 438 Astron. Soc., 476, 2220, doi: [10.1093/mnras/sty411](https://doi.org/10.1093/mnras/sty411)
- 439 Liao, K., Biesiada, M., & Zhu, Z.-H. 2022, Chin. Phys.
 440 Lett., 39, 119801, doi: [10.1088/0256-307X/39/11/119801](https://doi.org/10.1088/0256-307X/39/11/119801)
- 441 Liu, A., & Kim, K. 2024, Phys. Rev. D, 110, 123008,
 442 doi: [10.1103/PhysRevD.110.123008](https://doi.org/10.1103/PhysRevD.110.123008)
- 443 Liu, A., Wong, I. C. F., Leong, S. H. W., et al. 2023, Mon.
 444 Not. Roy. Astron. Soc., 525, 4149,
 445 doi: [10.1093/mnras/stad1302](https://doi.org/10.1093/mnras/stad1302)
- 446 Liu, X., Magana Hernandez, I., & Creighton, J. 2021,
 447 Astrophys. J., 908, 97, doi: [10.3847/1538-4357/abd7eb](https://doi.org/10.3847/1538-4357/abd7eb)
- 448 Lo, R. K. L., & Magaña Hernandez, I. 2021.
 449 <https://arxiv.org/abs/2104.09339>
- 450 Mapelli, M., Bouffanais, Y., Santoliquido, F., Arca Sedda,
 451 M., & Artale, M. C. 2022, Monthly Notices of the Royal
 452 Astronomical Society, 511, 5797–5816,
 453 doi: [10.1093/mnras/stac422](https://doi.org/10.1093/mnras/stac422)
- 454 Meena, A. K., Mishra, A., More, A., Bose, S., & Bagla,
 455 J. S. 2022, Mon. Not. Roy. Astron. Soc., 517, 872,
 456 doi: [10.1093/mnras/stac2721](https://doi.org/10.1093/mnras/stac2721)
- 457 Mishra, A., Meena, A. K., More, A., Bose, S., & Bagla,
 458 J. S. 2021, Mon. Not. Roy. Astron. Soc., 508, 4869,
 459 doi: [10.1093/mnras/stab2875](https://doi.org/10.1093/mnras/stab2875)
- 460 Nakamura, T. T. 1998, Phys. Rev. Lett., 80, 1138,
 461 doi: [10.1103/PhysRevLett.80.1138](https://doi.org/10.1103/PhysRevLett.80.1138)
- 462 Nakamura, T. T., & Deguchi, S. 1999, Progress of
 463 Theoretical Physics Supplement, 133, 137,
 464 doi: [10.1143/PTPS.133.137](https://doi.org/10.1143/PTPS.133.137)
- 465 Oguri, M. 2019, Rept. Prog. Phys., 82, 126901,
 466 doi: [10.1088/1361-6633/ab4fc5](https://doi.org/10.1088/1361-6633/ab4fc5)
- 467 Pang, P. T. H., Hannuksela, O. A., Dietrich, T., Pagano,
 468 G., & Harry, I. W. 2020, Monthly Notices of the Royal
 469 Astronomical Society, 495, 3740–3750,
 470 doi: [10.1093/mnras/staa1430](https://doi.org/10.1093/mnras/staa1430)
- 471 Portegies Zwart, S. F., & McMillan, S. L. W. 2000, ApJL,
 472 528, L17, doi: [10.1086/312422](https://doi.org/10.1086/312422)
- 473 Rodriguez, C. L., Haster, C.-J., Chatterjee, S., Kalogera,
 474 V., & Rasio, F. A. 2016, The Astrophysical Journal
 475 Letters, 824, L8, doi: [10.3847/2041-8205/824/1/l8](https://doi.org/10.3847/2041-8205/824/1/l8)
- 476 Schneider, P., Ehlers, J., & Falco, E. E. 1992, in
 477 Gravitational Lenses (Springer), 467–515
- 478 Schneider, P., Ehlers, J., & Falco, E. E. 1992, Gravitational
 479 Lenses, doi: [10.1007/978-3-662-03758-4](https://doi.org/10.1007/978-3-662-03758-4)
- 480 Seo, E., Shan, X., Januart, J., et al. 2025, Astrophys. J.,
 481 988, 159, doi: [10.3847/1538-4357/ade4bf](https://doi.org/10.3847/1538-4357/ade4bf)
- 482 Shan, X., Chen, X., Hu, B., & Cai, R.-G. 2023a.
 483 <https://arxiv.org/abs/2301.06117>
- 484 Shan, X., Chen, X., Hu, B., & Li, G. 2024, Sci. China Phys.
 485 Mech. Astron., 67, 269511,
 486 doi: [10.1007/s11433-023-2334-9](https://doi.org/10.1007/s11433-023-2334-9)
- 487 Shan, X., Li, G., Chen, X., et al. 2025, Sci. China Phys.
 488 Mech. Astron., 68, 219512,
 489 doi: [10.1007/s11433-024-2502-1](https://doi.org/10.1007/s11433-024-2502-1)
- 490 Shan, X., Li, G., Chen, X., Zheng, W., & Zhao, W. 2023b,
 491 Sci. China Phys. Mech. Astron., 66, 239511,
 492 doi: [10.1007/s11433-022-1985-3](https://doi.org/10.1007/s11433-022-1985-3)
- 493 Sigurdsson, S., & Hernquist, L. 1993, Nature, 364, 423,
 494 doi: [10.1038/364423a0](https://doi.org/10.1038/364423a0)
- 495 Spera, M., Mapelli, M., & Bressan, A. 2015, MNRAS, 451,
 496 4086, doi: [10.1093/mnras/stv1161](https://doi.org/10.1093/mnras/stv1161)
- 497 Takahashi, R., & Nakamura, T. 2003, Astrophys. J., 595,
 498 1039, doi: [10.1086/377430](https://doi.org/10.1086/377430)
- 499 Vernardos, G. 2018, Monthly Notices of the Royal
 500 Astronomical Society, 483, 5583,
 501 doi: [10.1093/mnras/sty3486](https://doi.org/10.1093/mnras/sty3486)
- 502 Wambsganss, J. 1990, Dissertation for doctoral degree,
 503 Munich University
- 504 Wierda, A. R. A. C., Wempe, E., Hannuksela, O. A.,
 505 Koopmans, L. e. V. E., & Van Den Broeck, C. 2021,
 506 Astrophys. J., 921, 154, doi: [10.3847/1538-4357/ac1bb4](https://doi.org/10.3847/1538-4357/ac1bb4)
- 507 Xu, F., Ezquiaga, J. M., & Holz, D. E. 2022, Astrophys. J.,
 508 929, 9, doi: [10.3847/1538-4357/ac58f8](https://doi.org/10.3847/1538-4357/ac58f8)
- 509 Zheng, W., Chen, X., Li, G., & Chen, H.-Z. 2022, An
 510 Improved GPU-Based Ray-Shooting Code For
 511 Gravitational Microlensing, arXiv,
 512 doi: [10.48550/ARXIV.2204.10871](https://doi.org/10.48550/ARXIV.2204.10871)